GEOLOGY | THE GEOLOGICAL SOCIETY OF AMERICA®

https://doi.org/10.1130/G53708.1

Manuscript received 3 July 2025
Revised manuscript received 4 November 2025
Manuscript accepted 17 November 2025

Published online 11 December 2025

Lithium isotopes reveal enhanced weathering fluxes in North America during the Paleocene–Eocene Thermal Maximum

Rocio Jaimes-Gutierrez[1,*], Lucas Vimpere[1], David J. Wilson[2], Patrick Blaser[3,4], Philip A.E. Pogge von Strandmann[2,5], Thierry Adatte[3], Swapan Sahoo[6], and Sébastien Castelltort[1]

[1]Department of Earth Sciences, University of Geneva, Rue des Maraîchers 13, 1205 Geneva, Switzerland
[2]London Geochemistry and Isotope Centre (LoGIC), Institute of Earth and Planetary Sciences, University College London, and Birkbeck University of London, Gower Street, London WC1E 6BT, UK
[3]Institute of Earth Sciences, University of Lausanne, Géopolis, 1015 Lausanne, Switzerland
[4]GEOMAR Helmholtz Centre for Ocean Research Kiel, Wischhofstrasse 1-3, 24148 Kiel, Germany
[5]Mainz Isotope and Geochemistry Centre (MIGHTY), Institute of Geosciences, Johannes Gutenberg University Mainz, J.-J.-Becher-Weg 21, 55128 Mainz, Germany
[6]Equinor, 2107 City West Boulevard, Suite 100, Houston, Texas 77042, USA

ABSTRACT

Silicate weathering regulates Earth's long-term climate by removing atmospheric CO_2. Understanding changes in weathering regimes and rates is key to predicting climate response time scales. We investigated the reactivity of the North American source-to-sink system and the chemical weathering regime during the Paleocene–Eocene Thermal Maximum (PETM). We measured the detrital lithium isotope composition (δ^7Li) in a deep-marine sediment core from the Gulf of Mexico, tracking changes in the formation of clay minerals, alongside neodymium isotopes (ε_{Nd}), to constrain sediment provenance. We find a buffered negative δ^7Li excursion during the PETM body, likely reflecting the mixing of neoformed and reworked clays from continental floodplains, followed by a stronger negative δ^7Li excursion during the recovery phase. This pattern aligns with the continental Bighorn Basin (Wyoming, USA) δ^7Li record, indicating rapid propagation of enhanced weathering and erosion fluxes in response to the PETM, which would have contributed to efficient CO_2 drawdown.

INTRODUCTION

The Paleocene–Eocene Thermal Maximum (PETM) was an ~170-kyr-long period of rapid (<5 kyr; Zeebe et al., 2016) global warming (5–9 °C; Thomas et al., 2002) that occurred 56 Ma ago (Röhl et al., 2007). Isotopically light carbon emissions drove a negative carbon isotope (δ^{13}C) excursion (CIE) featuring three phases (McInerney and Wing, 2011): (1) the onset, a period from the last pre-CIE to the most depleted isotope values; (2) the body, an interval of low and stable isotope values; and (3) the recovery, during which these values progressively returned to pre-PETM levels. In North America, the warming triggered more extreme and episodic rainfall and enhanced seasonality, thereby affecting water availability (Rush et al., 2021). These variations changed sediment transport dynamics, increasing denudation, especially along the North Atlantic margins (John et al., 2012). Kaolinite peaks at the PETM onset in many continental margin records suggest intensified chemical weathering and/or erosion of pre-PETM clays (e.g., Bolle and Adatte, 2001; John et al., 2012). Such mineralogical shifts may reflect intensified silicate weathering under a kinetically limited weathering regime, although regional responses may vary depending on local erosion rates, climate, and lithology (West et al., 2005).

Silicate weathering modulates atmospheric CO_2 drawdown over geological time scales (Walker et al., 1981). Marine carbonate records document enhanced weathering fluxes during the PETM (Pogge von Strandmann et al., 2021). In North America, climate-driven coupling between hydrological changes and weathering is recorded in continental interiors (Kraus et al., 2015; Ramos et al., 2022; Ji et al., 2023) and along the continental margin (Hessler et al., 2017). In the Bighorn Basin (Wyoming, USA), paleosols and carbonate/iron nodules suggest a decrease in mean annual precipitation and increased seasonality during the PETM onset and body. The resulting changes toward more shallow-rooted vegetation led to enhanced erosion rates, presumably outpacing weathering processes in the continental interior (McInerney and Wing, 2011; Wing and Currano, 2013; Ji et al., 2023). Deep-rooted vegetation returned during the recovery under wetter conditions with sustained seasonality (Wing and Currano, 2013).

Lithium (Li) isotopes trace silicate weathering, as clays preferentially take up ^{6}Li, causing the residual water to become isotopically heavy. Solution Li isotope compositions are therefore related to silicate weathering intensity (*W*/*D*), expressed as the weathering rate (*W*) over the denudation rate (*D*), where $D = W + E$, and *E* is erosion rate, in a "boomerang" shape (Dellinger et al., 2015). At low *W*/*D* (kinetically limited; congruent weathering), erosion rates and depths of erosion are high, water-rock interaction durations are limited, and $\delta^7Li_{solution}$ is low. At intermediate *W*/*D* (e.g., floodplains with extensive clay formation; incongruent weathering), $\delta^7Li_{solution}$ is high. At high *W*/*D* (supply-limited regimes like rainforests), fresh rock is scarce, and clay re-dissolution lowers $\delta^7Li_{solution}$, despite low weathering fluxes. Clays inherit Li from solution with an approximately constant fractionation, thereby mimicking the dissolved Li isotope "boomerang" pattern as a function of *W*/*D* (Pogge von Strandmann et al., 2023).

Rocio Jaimes-Gutierrez https://orcid.org/0000-0001-8649-2568
*rocio.jaimesgutierrez@unige.ch

CITATION: Jaimes-Gutierrez, R., et al., 2025, Lithium isotopes reveal enhanced weathering fluxes in North America during the Paleocene–Eocene Thermal Maximum: Geology, v. XX, p. , https://doi.org/10.1130/G53708.1

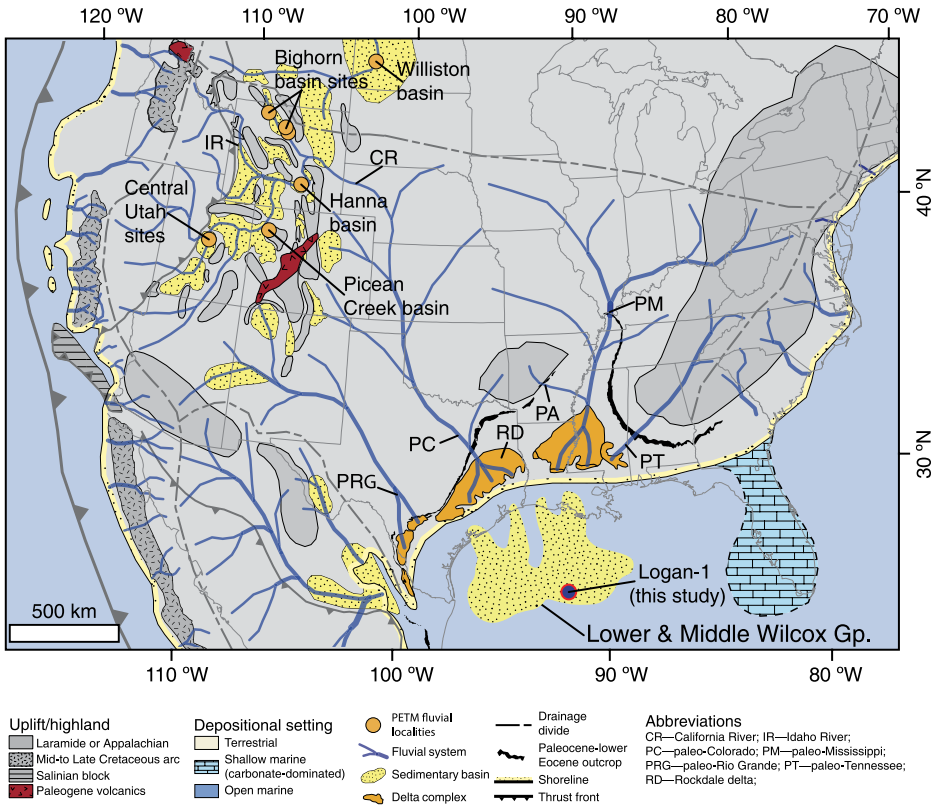

Figure 1. Location of the deep-water Logan-1 well (drilled by the drill ship *Discoverer Americas* in 2011 in the Gulf of Mexico) and paleogeographic reconstruction during the late Paleocene (modified from Sharman et al., 2017). Gp.—Group.

Bulk river sediments only partially reflect this trend due to mixing with unweathered silicates, especially at low *W/D* (Dellinger et al., 2017) (see Supplemental Material[1]).

Provenance tracers such as Nd isotopes help separate weathering shifts from lithological controls (Bayon et al., 2015), such that combined δ^7Li and ε_{Nd} records serve as a powerful proxy for weathering regime dynamics (Dellinger et al., 2017) (see methods in the Supplemental Material). After correcting $\delta^7Li_{detrital}$ for bedrock composition, $\Delta^7Li_{detrital\text{-}source}$ reflects *W/D* relative to modern river systems (Dellinger et al., 2015). Low δ^7Li_{clay} values in continental records are linked to hydroclimate changes during the PETM (Ramos et al., 2022). Negative $\delta^7Li_{carbonate}$ excursions in marine sections support increased silicate weathering fluxes at a global scale (Pogge von Strandmann et al., 2021). However, knowledge of how regional processes integrate into continental-scale denudation, and how the signal evolves from the terrestrial domain into the marine basin, is lacking.

[1]Supplemental Material. Setting, clay mineralogy, materials and methods, weathering interpretative framework, provenance and parent lithology, and geochemical analytical results (C, Li, and Nd isotopes). Please visit https://doi.org/10.1130/GEOL.S.30680759 to access the supplemental material; contact editing@geosociety.org with any questions.

We report a new Li isotope ($\delta^7Li_{detrital}$ and $\Delta^7Li_{detrital\text{-}source}$) and ε_{Nd} record from bulk sediments in a deep-water well core, the Logan-1 well in the Gulf of Mexico (Fig. 1; see Supplemental Material for setting). We assessed the chemical weathering regime during the pre-, syn- (body), recovery, and post-PETM periods, and compared the results to an existing regional continental record from the Bighorn Basin (Ramos et al., 2022) to evaluate the continental-scale signal propagation and weathering flux evolution.

RESULTS

Our measured $\delta^7Li_{detrital}$ values average 1.4‰ ± 0.6‰ (1 standard deviation [sd], n = 18) over the entire section (7840–8300 m; Fig. 2); 2.2‰ ± 0.2‰ during pre-PETM (8251–8196 m); 1.8‰ ± 0.3‰ during syn-PETM (8193–8062 m); 0.7‰ ± 0.2‰ during recovery (8059–7934 m); and 1.2‰ ± 0.5‰ post-PETM (7931–7684 m). The mean ε_{Nd} values are −13.1 ± 1.3 (1 sd, entire section, n = 22) (Fig. 2); −12.7 ± 0.5 (pre-PETM); −12.5 ± 1.8 (syn-PETM); −14.1 ± 0.3 (recovery); and −12.6 ± 0.1 (post-PETM). Syn-PETM $\delta^7Li_{detrital}$ values remained constant despite higher ε_{Nd} variability (Fig. 3A). For a given ε_{Nd} value during the recovery phase, $\delta^7Li_{detrital}$ values show a distinct 1.1‰ shift from syn-PETM, and 1.5‰ relative to pre-PETM values.

PROVENANCE AND PARENT LITHOLOGY CORRECTION

The Mesozoic Laramide orogeny initiated Laramide-sourced sediment influx into the Gulf of Mexico. By the Late Paleocene, drainage extended to northwestern North America (Bighorn Basin), bypassing hinterland basins (Galloway et al., 2011; Blum and Pecha, 2014; Sharman et al., 2017). Early Eocene tectonic shifts rerouted sediments via the Colorado and Rio Grande Rivers, reducing input along the Mississippi River axis (Galloway et al., 2011; Sharman et al., 2017). The PETM climate changes enhanced floodplain clay transport (Foreman, 2014; Barefoot et al., 2022), which bypassed the shelf through submarine canyons to form the Yoakum Shale (Vimpere et al., 2023).

Despite these rearrangements, provenance studies show that the Wilcox Group was primarily sourced from the Western Cordillera and Laramide crystalline highlands (Sharman et al., 2017; Vimpere et al., 2023), with ε_{Nd} values supporting constant provenance (Fig. 2F). Minor Appalachian-Grenville input (Blum and Pecha, 2014) reflects reworking of older sediments in the eastern interior (Sharman et al., 2017), potentially serving as CO_2 sources (Hollingsworth et al., 2024). We applied a parent lithology correction (see the Supplemental Material and Figure S2 therein) and obtain a pre-PETM $\Delta^7Li_{detrital\text{-}source}$ of −1.8‰ ± 0.2‰, syn-PETM of −2.2‰ ± 0.3‰, recovery of −3.3‰ ± 0.2‰, and post-PETM of −2.8‰ ± 0.5‰.

WEATHERING EVOLUTION IN THE NORTH AMERICAN INTERIOR

Diverse pre-PETM climates prevailed across North America, with temperate conditions in the northwestern interior, subtropical conditions in the southwestern interior, and an orographic monsoonal tropical regime at the Colorado Front Range (Sewall and Sloan, 2006; Tierney et al., 2022). Overall, the paleo-Colorado catchment experienced temperate to tropical weathering conditions (Hessler et al., 2017).

During the PETM, warmer and drier conditions prevailed, with increased precipitation seasonality and higher monsoonal discharge along the Rocky Mountains (Kraus et al., 2015). Elevated sedimentation rates in the Gulf of Mexico (Cunningham et al., 2022) are consistent with doubled erosion rates compared to the late Paleocene, with a system-clearing event transporting large dissolved and sediment loads to the oceans (Foreman et al., 2012). In the Bighorn Basin, these environmental conditions were interpreted to have enhanced clay formation (Ramos et al., 2022), which was recorded to a diminished degree in the negative $\delta^7Li_{detrital}$ excursion in the Logan-1 well (Fig. 2).

The recovery phase saw a return to wetter conditions, although the climate remained warm

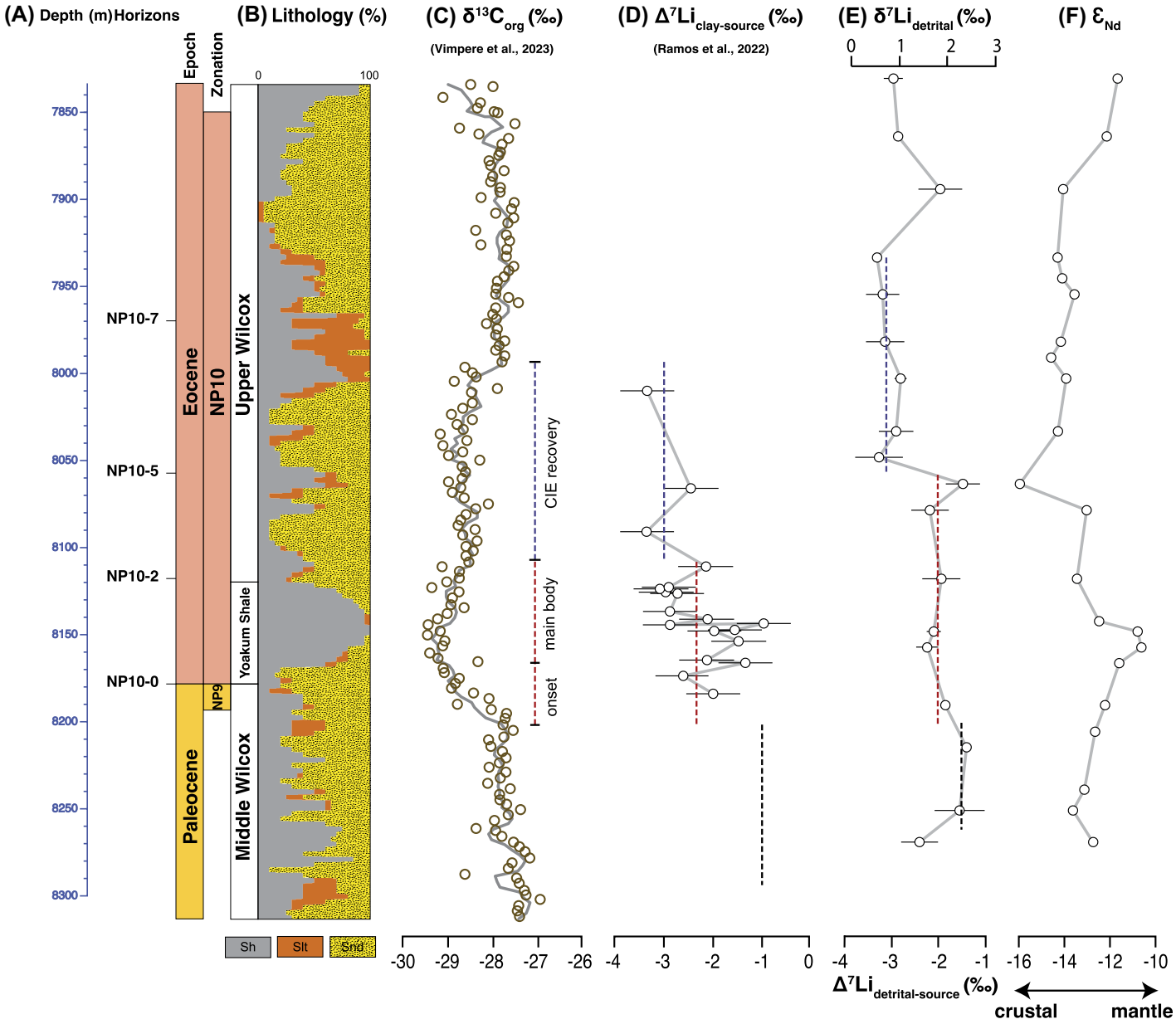

Figure 2. Records of erosion and weathering changes from the Gulf of Mexico and the Bighorn Basin (Wyoming, USA). (A) Depth and horizons. (B) Lithology. (C) $\delta^{13}C_{org}$ record from Vimpere et al. (2023). (D) $\Delta^{7}Li_{clay\text{-}source}$ from the Bighorn Basin (Ramos et al., 2022), compared to (E) $\delta^{7}Li_{detrital}$ and $\Delta^{7}Li_{detrital\text{-}source}$, and (F) ε_{Nd} from the sediment core of the deep-water Logan-1 well (Gulf of Mexico; this study). Analytical uncertainties (2 sd) for $\delta^{7}Li$ are shown as error bars; for ε_{Nd}, they are smaller than the symbol size. Data from the Logan-1 well are on a depth scale, and data from the Bighorn Basin are aligned using Paleocene–Eocene Thermal Maximum (PETM) time constraints. Pre-PETM values in the Bighorn Basin are not displayed due to the lack of a calibrating lower-age boundary. CIE—carbon isotope ($\delta^{13}C$) excursion; Sh—shale; Slt—silt; Snd—sand.

and seasonally wet (Kraus and Riggins, 2007; Kraus et al., 2015). Sediment supply to the Gulf of Mexico declined due to sediment trapping in intra-foreland basins and resumed progradation of deltaic systems (Galloway et al., 2011).

Stable ε_{Nd} values (Fig. 3A) indicate consistent sediment sourcing, suggesting that sedimentation changes were climatically driven rather than provenance driven, consistent with stable late Paleocene drainage networks (Blum and Pecha, 2014). The Bighorn Basin record (Ramos et al., 2022), representing the upstream catchment area, shows lower $\delta^{7}Li_{clay}$ values for both syn-PETM and the recovery phase relative to pre-PETM conditions (Fig. 2D), supporting enhanced rock dissolution inferred from the negative $\delta^{7}Li_{detrital}$ excursion in the Gulf of Mexico record (Fig. 2E).

The synchronous $\delta^{7}Li_{detrital}$ shift at the PETM onset in both the Bighorn Basin and the Gulf of Mexico (Fig. 2) indicates strong system connectivity from northwestern North America to the deep marine basin (Sharman et al., 2017). The syn-PETM excursion is smaller in the Gulf of Mexico than upstream (Ramos et al., 2022), likely due to dilution of the newly formed PETM clays with pre-PETM clays, resulting in a muted isotopic signal. Enhanced clay export driven by vegetation changes (Wing and Currano, 2013), greater channel mobility and more frequent avulsions (Barefoot et al., 2022), and excavation of the Yoakum Canyon (the largest Gulf Coast Eocene erosional gorge) with remobilization of Lower Wilcox distal deltaic sediments (Vimpere et al., 2023) may have further buffered the signal.

During the recovery phase, increased rainfall with sustained seasonality (Kraus and Riggins, 2007; Kraus et al., 2015) and denser deep-rooted vegetation (McInerney and Wing, 2011) reduced channel mobility and decreased the reworking of floodplain clays. The reduced dilution of neoformed PETM clays could have

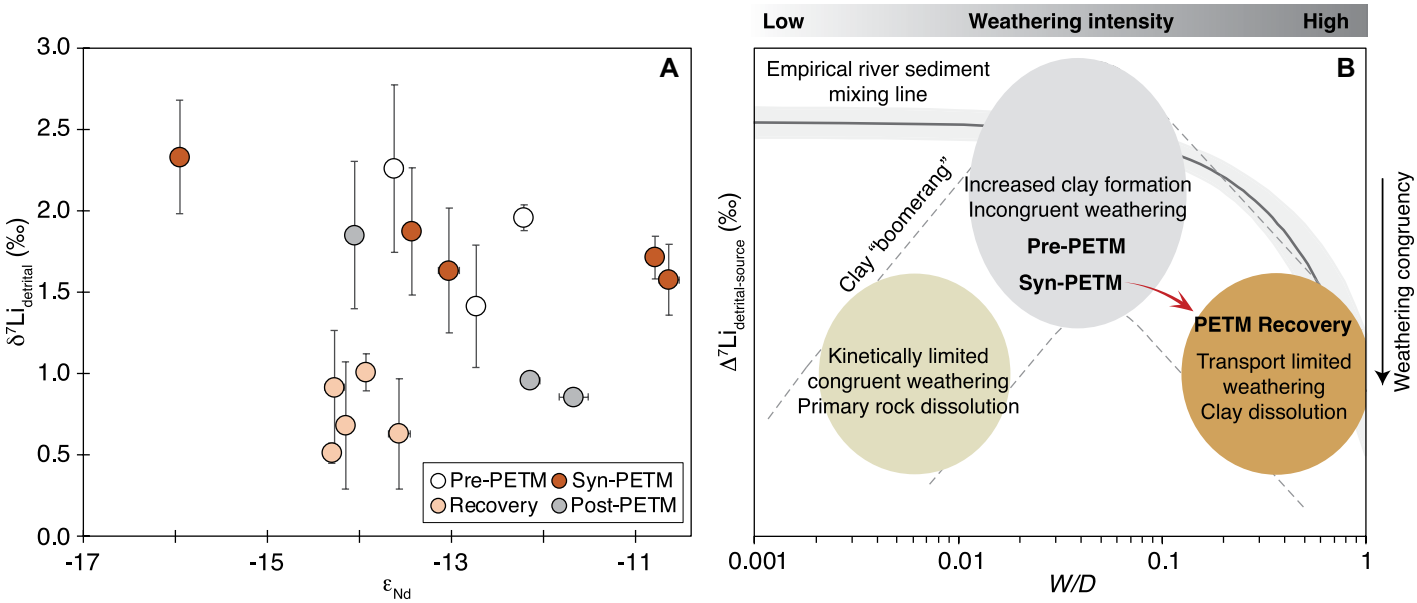

Figure 3. (A) $\delta^7Li_{detrital}$ versus ε_{Nd} values on decarbonated bulk sediment, showing no correlation for pre- or syn-Paleocene–Eocene Thermal Maximum (PETM). The recovery phase reflects a −1.1 ‰ excursion from syn-PETM values and −1.5 ‰ relative to pre-PETM values. (B) Schematic $\Delta^7Li_{detrital\text{-}source}$ versus silicate weathering intensity (*W*/*D*), expressed as the weathering rate (*W*) over the denudation rate (*D*), where $D = W + E$, and *E* is erosion rate. The pre- to syn-PETM shows a dampened shift toward more negative values. The syn-PETM to recovery suggests a shift toward higher *W*/*D* under subdued *E*. Modified from Dellinger et al. (2015, 2017).

produced the stronger negative $\delta^7Li_{detrital}$ shift (Fig. 2), better reflecting the true weathering conditions at the time.

Alternatively, an ~100 kyr lag time in the weathering signal propagation from the continent to the deep marine basin (Röhl et al., 2007) would place the main PETM weathering phase in the recovery interval. Ji et al. (2023) recorded a detrital smectite increase in the Bighorn Basin during the PETM, with an ~20 kyr lag and an ~50 kyr duration, consistent with some transfer delay. However, the synchronicity of the CIE and the Li isotope excursion at the PETM onset, both upstream and downstream (Fig. 2), makes this scenario unlikely. Additionally, immediate signal propagation is consistent with the theoretical transport time for mud-rich sediments to the Gulf of Mexico of a few weeks (Tofelde et al., 2021), with an upper boundary for the sediment transport lag time of ~10 kyr (Dosseto et al., 2006). Thus, we favor the muted-body hypothesis, whereby channel mobility and reworking partly buffered the syn-PETM *W*/*D* signal.

The δ^7Li record shows a muted syn-PETM change and a negative excursion during the recovery, indicating a shift from high erosion and weathering fluxes to a higher *W*/*D* regime as erosion subsided (Fig. 3B). Global erosion rates are estimated to have risen 2- to 3-fold during the PETM (Pogge von Strandmann et al., 2021). While North America lacks direct quantification, indirect proxies support this estimate at the continent scale, such as a modeled ~37% increase in annual runoff in the western Mid-Atlantic (Rush et al., 2021) and an observed ~5-fold increase in regional sedimentation rates in the Gulf of Mexico (Cunningham et al., 2022). Assuming the Laramide uplift was the main source of sediments for the Gulf of Mexico, low-temperature thermochronology data suggest a 2- to 3-fold erosion rate increase when averaged over the drainage area (Fig. 1) (Jepson et al., 2025). To maintain an approximately constant *W*/*D* these erosion rates would suggest a proportional increase in weathering fluxes. Osmium isotope mass-balance modeling shows that global silicate weathering fluxes increased by only ~35%–40% (Tanaka et al., 2000). Such a modest increase in *W*, relative to larger increases in *D*, further supports an overall global decrease in *W*/*D* and a shift toward a climate sensitive, kinetically limited regime. Under such conditions, primary silicate dissolution would outpace clay formation, and the efficient CO_2 sink would aid climate recovery. During the recovery phase, reduced erosion and an undiluted $\delta^7Li_{detrital}$ excursion point to higher *W*/*D* conditions. The rise in illite (Fig. S1; Vimpere et al., 2023) likely reflects continued sediment supply and evolving clay assemblages under warm, humid conditions. Additional carbon fluxes also warrant consideration: erosion of sedimentary rocks may have led to oxidation of petrogenic carbon, acting as a CO_2 source, while increased terrigenous sediment export likely enhanced organic carbon burial, acting as a sink (Hollingsworth et al., 2024). These processes remain key uncertainties in PETM carbon cycling.

CONCLUSIONS

Our geochemical records from the Gulf of Mexico integrate the complexity of varying climatic responses across the North American interior. The $\delta^7Li_{detrital}$ record exhibits a muted excursion during the syn-PETM, followed by a stronger negative excursion during the recovery phase, consistent with the Bighorn Basin continental record. We interpret the first step as reflecting an erosion-driven increase in total weathering fluxes during the PETM body, with rapid denudation enhancing primary silicate dissolution and CO_2 drawdown. The second step indicates a recovery-phase shift toward higher *W*/*D* as erosion rates declined. Although previous global estimates suggest only a modest ~35%–40% increase in global silicate weathering fluxes, our data indicate that continental interiors such as North America experienced transient, but efficient, silicate weathering responses that contributed to climate recovery. The parallel evolution of Li isotopes in both continental and marine settings demonstrates the rapid propagation of weathering signals through sediment-routing systems, and underscores the climatic coupling between upland erosion, lowland weathering, and global carbon cycling during the PETM.

ACKNOWLEDGMENTS

S. Castelltort obtained funding from the European Union's Horizon 2020 research and innovation programme, and P. Blaser obtained funding from Horizon Europe, under the Marie Sklodowska-Curie grant agreement numbers 860383 and 101065424, respectively. D.J. Wilson was supported by a Natural Environment Research Council (NERC) independent research fellowship (NE/T011440/1). We thank R.G. Hilton, E.J. Ramos, and an anonymous reviewer for their constructive comments that helped improve the manuscript.

REFERENCES CITED

Barefoot, E.A., Nittrouer, J.A., Foreman, B.Z., Hajek, E.A., Dickens, G.R., Baisden, T., and Toms, L., 2022, Evidence for enhanced fluvial channel mobility and fine sediment export due to precipitation seasonality during the Paleocene-Eocene thermal maximum: Geology, v. 50, p. 116–120, https://doi.org/10.1130/G49149.1.

Bayon, G., et al., 2015, Rare earth elements and neodymium isotopes in world river sediments revisited: Geochimica et Cosmochimica Acta, v. 170, p. 17–38, https://doi.org/10.1016/j.gca.2015.08.001.

Blum, M., and Pecha, M., 2014, Mid-Cretaceous to Paleocene North American drainage reorganization from detrital zircons: Geology, v. 42, p. 607–610, https://doi.org/10.1130/G35513.1.

Bolle, M.-P., and Adatte, T., 2001, Palaeocene-early Eocene climatic evolution in the Tethyan realm: Clay mineral evidence: Clay Minerals, v. 36, p. 249–261, https://doi.org/10.1180/000985501750177979.

Cunningham, R., Phillips, M.P., Snedden, J.W., Norton, I.O., Lowery, C.M., Virdell, J.W., Barrie, C.D., and Avery, A., 2022, Productivity and organic carbon trends through the Wilcox Group in the deep Gulf of Mexico: Evidence for ventilation during the Paleocene-Eocene Thermal Maximum: Marine and Petroleum Geology, v. 140, https://doi.org/10.1016/j.marpetgeo.2022.105634.

Dellinger, M., Gaillardet, J., Bouchez, J., Calmels, D., Louvat, P., Dosseto, A., Gorge, C., Alanoca, L., and Maurice, L., 2015, Riverine Li isotope fractionation in the Amazon River basin controlled by the weathering regimes: Geochimica et Cosmochimica Acta, v. 164, p. 71–93, https://doi.org/10.1016/j.gca.2015.04.042.

Dellinger, M., Bouchez, J., Gaillardet, J., Faure, L., and Moureau, J., 2017, Tracing weathering regimes using the lithium isotope composition of detrital sediments: Geology, v. 45, p. 411–414, https://doi.org/10.1130/G38671.1.

Dosseto, A., Bourdon, B., Gaillardet, J., Maurice-Bourgoin, L., and Allegre, C., 2006, Weathering and transport of sediments in the Bolivian Andes: Time constraints from uranium-series isotopes: Earth and Planetary Science Letters, v. 248, p. 759–771, https://doi.org/10.1016/j.epsl.2006.06.027.

Foreman, B.Z., 2014, Climate-driven generation of a fluvial sheet sand body at the Paleocene–Eocene boundary in north-west Wyoming (USA): Basin Research, v. 26, p. 225–241, https://doi.org/10.1111/bre.12027.

Foreman, B.Z., Heller, P.L., and Clementz, M.T., 2012, Fluvial response to abrupt global warming at the Palaeocene/Eocene boundary: Nature, v. 491, p. 92–95, https://doi.org/10.1038/nature11513.

Galloway, W.E., Whiteaker, T.L., and Ganey-Curry, P., 2011, History of Cenozoic North American drainage basin evolution, sediment yield, and accumulation in the Gulf of Mexico basin: Geosphere, v. 7, p. 938–973, https://doi.org/10.1130/GES00647.1.

Hessler, A.M., Zhang, J., Covault, J., and Ambrose, W., 2017, Continental weathering coupled to Paleogene climate changes in North America: Geology, v. 45, p. 911–914, https://doi.org/10.1130/G39245.1.

Hollingsworth, E.H., Sparkes, R.B., Self-Trail, J.M., Foster, G.L., and Inglis, G.N., 2024, Enhanced petrogenic organic carbon oxidation during the Paleocene-Eocene thermal maximum: Geochemical Perspectives Letters, v. 33, p. 1–6, https://doi.org/10.7185/geochemlet.2444.

Jepson, G., Carrapa, B., Reeher, L.J., DeCelles, P.G., Afonso, W.D., Howlett, C.J., Caylor, E.A., Sherpa, T.Z.L., Wang, J.W., and Constenius, K.N., 2025, Regional exhumation of the Laramide Province: Geological Society of America Bulletin, v. 137, p. 2913–2932, https://doi.org/10.1130/B37625.1.

Ji, K., et al., 2023, Elevated physical weathering exceeds chemical weathering of clays during the Paleocene-Eocene Thermal Maximum in the continental Bighorn Basin (Wyoming, USA): Palaeogeography, Palaeoclimatology, Palaeoecology, v. 615, https://doi.org/10.1016/j.palaeo.2023.111445.

John, C.M., Banerjee, N.R., Longstaffe, F.J., Sica, C., Law, K.R., and Zachos, J.C., 2012, Clay assemblage and oxygen isotopic constraints on the weathering response to the Paleocene-Eocene thermal maximum, east coast of North America: Geology, v. 40, p. 591–594, https://doi.org/10.1130/G32785.1.

Kraus, M.J., and Riggins, S., 2007, Transient drying during the Paleocene–Eocene Thermal Maximum (PETM): Analysis of paleosols in the Bighorn Basin, Wyoming: Palaeogeography, Palaeoclimatology, Palaeoecology, v. 245, p. 444–461, https://doi.org/10.1016/j.palaeo.2006.09.011.

Kraus, M.J., Woody, D.T., Smith, J.J., and Dukic, V., 2015, Alluvial response to the Paleocene–Eocene Thermal Maximum climatic event, Polecat Bench, Wyoming (U.S.A.): Palaeogeography, Palaeoclimatology, Palaeoecology, v. 435, p. 177–192, https://doi.org/10.1016/j.palaeo.2015.06.021.

McInerney, F.A., and Wing, S.L., 2011, The Paleocene-Eocene Thermal Maximum: A perturbation of carbon cycle, climate, and biosphere with implications for the future: Annual Review of Earth and Planetary Sciences, v. 39, p. 489–516, https://doi.org/10.1146/annurev-earth-040610-133431.

Pogge von Strandmann, P.A.E., Jones, M.T., West, A.J., Murphy, M.J., Stokke, E.W., Tarbuck, G., Wilson, D.J., Pearce, C.R., and Schmidt, D.N., 2021, Lithium isotope evidence for enhanced weathering and erosion during the Paleocene-Eocene Thermal Maximum: Science Advances, v. 7, https://doi.org/10.1126/sciadv.abh4224.

Pogge von Strandmann, P.A.E., Cosford, L.R., Liu, C.-Y., Liu, X., Krause, A.J., Wilson, D.J., He, X., McCoy-West, A.J., Gislason, S.R., and Burton, K.W., 2023, Assessing hydrological controls on the lithium isotope weathering tracer: Chemical Geology, v. 642, https://doi.org/10.1016/j.chemgeo.2023.121801.

Ramos, E.J., et al., 2022, Swift weathering response on floodplains during the Paleocene-Eocene Thermal Maximum: Geophysical Research Letters, v. 49, https://doi.org/10.1029/2021GL097436.

Röhl, U., Westerhold, T., Bralower, T.J., and Zachos, J.C., 2007, On the duration of the Paleocene-Eocene thermal maximum (PETM): Geochemistry, Geophysics, Geosystems, v. 8, Q12002, https://doi.org/10.1029/2007GC001784.

Rush, W.D., Kiehl, J.T., Shields, C.A., and Zachos, J.C., 2021, Increased frequency of extreme precipitation events in the North Atlantic during the PETM: Observations and theory: Palaeogeography, Palaeoclimatology, Palaeoecology, v. 568, https://doi.org/10.1016/j.palaeo.2021.110289.

Sewall, J.O., and Sloan, L.C., 2006, Come a little bit closer: A high-resolution climate study of the early Paleogene Laramide foreland: Geology, v. 34, p. 81–84, https://doi.org/10.1130/G22177.1.

Sharman, G.R., Covault, J.A., Stockli, D.F., Wroblewski, A.F.-J., and Bush, M.A., 2017, Early Cenozoic drainage reorganization of the United States Western Interior–Gulf of Mexico sediment routing system: Geology, v. 45, p. 187–190, https://doi.org/10.1130/G38765.1.

Tanaka, T., et al., 2000, JNdi-1: A neodymium isotopic reference in consistency with LaJolla neodymium: Chemical Geology, v. 168, p. 279–281, https://doi.org/10.1016/S0009-2541(00)00198-4; erratum available at https://doi.org/10.1575/1912/bco-dmo.788195.1.

Thomas, D.J., Zachos, J.C., Bralower, T.J., Thomas, E., and Bohaty, S., 2002, Warming the fuel for the fire: Evidence for the thermal dissociation of methane hydrate during the Paleocene-Eocene thermal maximum: Geology, v. 30, p. 1067–1070, https://doi.org/10.1130/0091-7613(2002)030<1067:WTFFTF>2.0.CO;2.

Tierney, J.E., Zhu, J., Li, M., Ridgwell, A., Hakim, G.J., Poulsen, C.J., Whiteford, R.D.M., Rae, J.W.B., and Kump, L.R., 2022, Spatial patterns of climate change across the Paleocene–Eocene Thermal Maximum: Proceedings of the National Academy of Sciences of the United States of America, v. 119, https://doi.org/10.1073/pnas.2205326119.

Tofelde, S., Bernhardt, A., Guerit, L., and Romans, B.W., 2021, Times associated with source-to-sink propagation of environmental signals during landscape transience: Frontiers of Earth Science, v. 9, https://doi.org/10.3389/feart.2021.628315.

Vimpere, L., et al., 2023, Carbon isotope and biostratigraphic evidence for an expanded Paleocene–Eocene Thermal Maximum sedimentary record in the deep Gulf of Mexico: Geology, v. 51, p. 334–339, https://doi.org/10.1130/G50641.1.

Walker, J.C.G., Hays, P.B., and Kasting, J.F., 1981, A negative feedback mechanism for the long-term stabilization of Earth's surface temperature: Journal of Geophysical Research: Oceans, v. 86, p. 9776–9782, https://doi.org/10.1029/JC086iC10p09776.

West, A., Galy, A., and Bickle, M., 2005, Tectonic and climatic controls on silicate weathering: Earth and Planetary Science Letters, v. 235, p. 211–228, https://doi.org/10.1016/j.epsl.2005.03.020.

Wing, S.L., and Currano, E.D., 2013, Plant response to a global greenhouse event 56 million years ago: American Journal of Botany, v. 100, p. 1234–1254, https://doi.org/10.3732/ajb.1200554.

Zeebe, R.E., Ridgwell, A., and Zachos, J.C., 2016, Anthropogenic carbon release rate unprecedented during the past 66 million years: Nature Geoscience, v. 9, p. 325–329, https://doi.org/10.1038/ngeo2681.

Printed in the USA

Jaimes-Gutierrez, R., et al., 2025, Lithium isotopes reveal enhanced weathering fluxes in North America during the Paleocene–Eocene Thermal Maximum: Geology, https://doi.org/10.1130/G53708.1

Supplemental Material

Setting, clay mineralogy, materials and methods, weathering interpretative framework, provenance and parent lithology, and geochemical analytical results (C, Li, and Nd isotopes).

SETTING

Analyses were conducted on a 543 m-thick section from the ultra-deepwater Wildcat Logan-1 well (drilled in 2011 on Walker Ridge Block 969, ID WR 969 STO #1; Fig. 1), including a 180 m-thick interval correlated with the PETM (Vimpere et al., 2023). The well was drilled on the outboard of the Wilcox Group, a prograding Paleocene-Eocene sequence comprising a deep turbiditic system in the GoM (Zarra, 2017). It connects to a Laramide orogeny-controlled continental-scale sediment routing system, mainly transporting sediments through the paleo-Rio Grande, Colorado, and Mississippi trunks (Sharman et al., 2017, 2023). Clay mineralogy is stable throughout the section, except for a decrease in smectite of 12 wt% from pre- to syn-PETM, coeval with an increase in chlorite during the body, followed by an increase in illite during the recovery (Fig. S1, Vimpere et al., 2023). The studied section comprises the Paleocene Middle Wilcox and the Eocene Yoakum Shale-Upper Wilcox complexes, deposited in a submarine fan setting.

CLAY MINERALOGY

The clay mineralogy (Vimpere et al., 2023, their Supplementary Table 1) was dominated by illite (43±12 wt%, 1sd), smectite (23±17 wt%), chlorite (20±8 wt%), and kaolinite (15±5 wt%) with a standard error (1se) of 1% (Fig. S1). Illite had a pre-PETM abundance of (42±8 wt%; 8251-8196 m), syn-PETM (44±9 wt%; 8193-8062 m), recovery (49±9 wt%; 8059-7934 m), and post-PETM (37±16 wt%; 7931-7684 m). Smectite had a pre-PETM abundance of (26±10 wt%), syn-PETM (16±5 wt%), recovery (13±5 wt%), and post-PETM (36±25 wt%). Chlorite had a pre-PETM abundance of (17±8 wt%), syn-PETM (24±8 wt%), recovery (23±7 wt%), and post-PETM (16±8 wt%). Kaolinite had a pre-PETM abundance of (15±5 wt%), syn-PETM (17±4 wt%), recovery (15±4 wt%), and post-PETM (12±6 wt%).

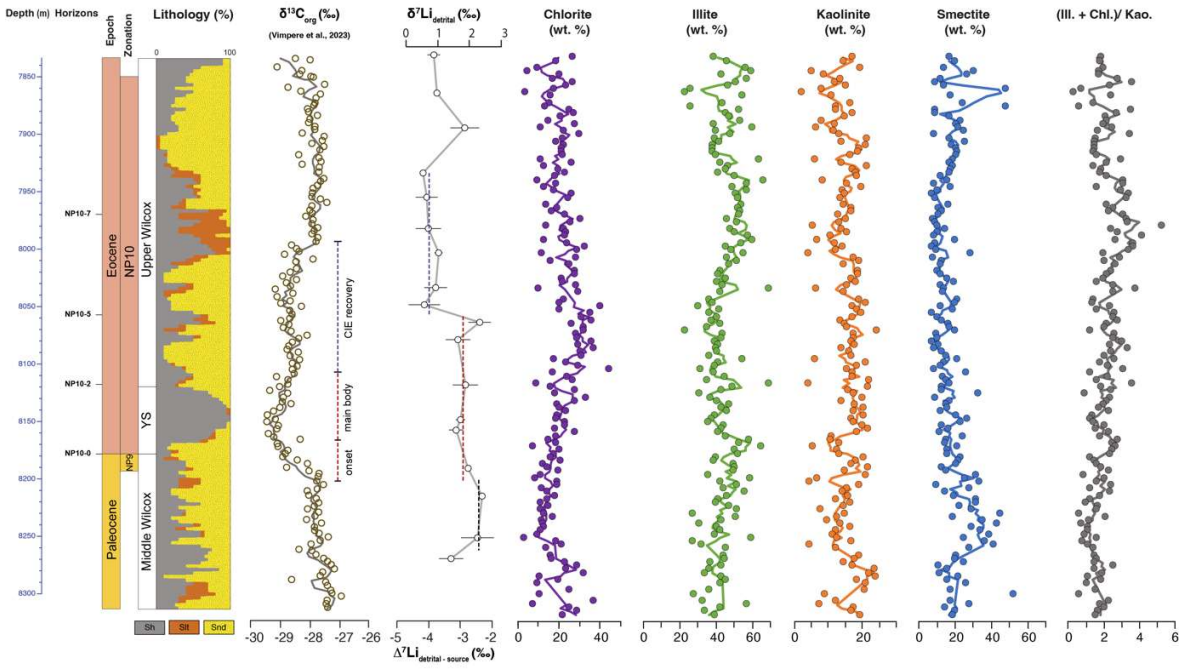

Figure S1. *Clay mineralogy in the Logan-1 well. Clay abundances were dominated by illite and smectite, with lower abundances of chlorite and kaolinite (Vimpere et al., 2023, their Supplementary Table 1).*

MATERIALS AND METHODS

Lithium isotopes

Samples (n = 18) were selected for Li isotope analysis based on their depth distribution along the section, prioritising intervals with high mud content from pre-, syn-, and post-PETM. Bulk detrital sediment samples were subjected to bulk digestion using concentrated HF, HNO_3, and $HClO_4$ in Teflon beakers on a hotplate at 130 °C, followed by steps in concentrated HNO_3 and 6 M HCl.

A standard method was applied for Li isotope separation in 0.2 M HCl, using two column passes through AG50W X-12 resin to ensure matrix removal (Pogge von Strandmann et al., 2013, 2021b). Splits were collected before and after the Li collection intervals to assess

column yields, as Li isotopes are fractionated during ion chromatography. Here, yields from the two combined column passes were 99.6–100%. A 1% loss in yield at UCL has been assessed to lead to an offset of 1.7‰ (Wilson et al., 2021). Isotope analyses were performed on a Nu Plasma 3 MC-ICP-MS at University College London's LOGIC laboratories, with normalisation to IRMM-016 bracketing standards, which are equivalent to LSVEC. Samples were measured at least three times within an analytical session, and the reported values are the mean and standard deviation (2sd) of these values. Accuracy and external reproducibility were assessed using full procedural replicate measurements of USGS standard BCR-2, which gave δ^7Li values of 2.1±0.5‰ (2sd, n = 9), consistent with previous results from this laboratory (2.5±0.3‰, 2sd, n = 5) (Wilson et al., 2021) and indicating a long-term reproducibility of ~0.5‰ (2sd). The mean procedural blank was 0.07 ng (range of 0.01−0.17 ng, n = 6), which was negligible compared to sample Li amounts (~200−400 ng) and hence did not warrant blank correction.

Neodymium isotopes

We also analysed the Nd isotope compositions of decarbonated sediment samples (n = 22) along the section. To this end, 50 mg of crushed samples were fully digested with a high-pressure microwave system, and Nd was purified with a two-step ion chromatographic procedure before its isotopic composition was analysed on a Thermo Scientific Neptune Plus MC-ICP-MS at the University of Lausanne, following Blaser et al. (2016). The $^{143}Nd/^{144}Nd$ ratios were corrected to a $^{146}Nd/^{144}Nd$ ratio of 0.7219 with the exponential law and normalised to JNdi-1 standards with $^{143}Nd/^{144}Nd$ = 0.512115 (Tanaka et al., 2000). Reproducibility was assessed by repeated measurements of secondary in-house solutions and was ±0.15 epsilon units (95% confidence).

WEATHERING EVOLUTION: LITHIUM ISOTOPE INTERPRETATIVE FRAMEWORK

Lithium (Li) isotopes trace silicate weathering, as clay formation preferentially takes up the light isotope (^{6}Li), driving the residual water isotopically heavy (^{7}Li). In a closed system, both the water and the clays precipitating from it become isotopically heavier with progressive weathering. Clays inherit the Li isotopic composition from solution, but offset based on an approximately constant fractionation factor $\alpha < 1$ (Pistiner and Henderson, 2003; Pogge von Strandmann et al., 2023). Hence, silicate weathering intensity, expressed as the weathering rate (W) over the denudation rate (D), where $D = W + E$ (erosion rate), exerts a main control on both solution and clay Li isotope compositions, forming a "boomerang" shape (Fig. 3B in main text) (Dellinger et al., 2015; Winnick et al., 2022; Pogge von Strandmann et al., 2023; Wei et al., 2025). However, bulk river sediments only partially reflect this trend due to mixing of the clays with unweathered primary silicates, especially at low W/D (Dellinger et al., 2017).

At low W/D (kinetically-limited; congruent weathering), erosion rates and depth of erosion are high. In this setting, secondary mineral formation is limited by the short mineral residence times in soils, generating low values for $\delta^7Li_{solution}$ that are close to $\delta^7Li_{bedrock}$ (Bouchez et al., 2013; Dellinger et al., 2015). The small quantities of secondary minerals formed in this setting have a low δ^7Li composition, which is reflected in the δ^7Li_{clay} (Dosseto et al., 2015). However, at very low weathering intensity ($W/D < 0.01$), typical of high-erosion settings, the detrital sediments carried by rivers contain a high proportion of primary minerals, making $\delta^7Li_{detrital}$ similar to $\delta^7Li_{bedrock}$ (Dellinger et al., 2017). At low W/D, W is kinetically-driven, and therefore depends on temperature and runoff, as well as other influences such as vegetation (West et al., 2005). At intermediate W/D (e.g. floodplains with high clay formation; incongruent weathering), $\delta^7Li_{solution}$ and $\delta^7Li_{detrital}$ are both high. Finally, at high W/D (supply-limited

regimes like rainforests), fresh rock is scarce, and clay re-dissolution lowers $\delta^7Li_{solution}$, despite low weathering fluxes. In modern rivers, high *W/D* values are only seen in the Amazon and Orinoco lowlands and the Congo River, all in supply-limited settings, with low erosion rates and deeply weathered soils. At low erosion rates, weathering rates vary predictably, scaling proportionally with erosion rates.

This behaviour provides two interpretative frameworks for Li isotopes in silicate sediment archives as paleo-weathering proxies: (A) the dissolved-load "boomerang" model, with a constant offset for clay minerals (Pogge von Strandmann et al., 2021b; Jones et al., 2023; Pogge von Strandmann et al., 2023; Ramos et al., 2024; Rush et al., 2025; Liu et al., 2025; Wei et al., 2025) and (B) the detrital bulk sediment relationship (clay + silt fractions) described by Dellinger et al. (2017) and further supported by Ramos et al. (2022) and Chen et al. (2023).

The selection of an interpretative framework must consider three key factors: (1) Grain size fraction analysed – therefore accounting for the degree of dilution due to primary silicates (Dellinger et al., 2017). Coarser size fractions will contain higher proportions of primary minerals, whereas finer size fractions will contain more secondary clays. (2) Hydrodynamic sorting – differential transport of clay minerals can influence Li isotopic signatures. Liu et al. (2023) demonstrated that mechanical sorting allows clays, due to their low settling velocities, to be transported further from river mouths, increasing the representation of isotopically light secondary clays relative to coarser silicates. (3) Bedrock lithology – the mimicking relationship between clays and the dissolved load for Li isotopes has been empirically demonstrated in volcanic terrains (e.g. Pogge von Strandmann et al., 2023; Ramos et al., 2024), where the high reactivity of primary minerals enhances isotopic fractionation during secondary mineral formation, but requires further exploration for other lithologies.

The boomerang framework is consistent with reactive transport and global river modelling studies, which show that the isotopic composition of the dissolved phase dominates the isotopic mass balance of continental Li export (Pogge von Strandmann et al., 2021a; Winnick et al., 2022; Ramos et al., 2024). In high-sediment-flux systems, rapid physical erosion and clay reworking can dampen the detrital Li isotope excursions but should not erase the underlying relationship between δ^7Li and *W/D* (Rush et al., 2025).

The archive analysed here consists of bulk detrital sediments that may include reworked pre- and syn-PETM material. However, given that the selected samples are mud-rich (Vimpere et al., 2023), and considering the likely influence of hydrodynamic sorting and distal transport processes (Liu et al., 2023), we propose that the dissolved-load boomerang model provides an appropriate framework for interpreting the Li isotope record. This approach accounts for both the inheritance of dissolved-load isotopic signatures by clays and the integrating nature of continental-scale sedimentary systems.

PROVENANCE AND PARENT LITHOLOGY CORRECTION

The Mesozoic subduction-driven Laramide orogeny (Heller and Liu, 2016) initiated Laramide-sourced sediment influx into the GoM. By the Late Paleocene, drainage capture extended to NW USA (Bighorn Basin), bypassing hinterland basins (Galloway et al., 2011; Blum and Pecha, 2014; Sharman et al., 2017; Pecha et al., 2022). Thus, the substantial increase in sediment supply starting in the Late Paleocene Lower Wilcox Group caused the progradation of the Colorado and Mississippi deltaic systems and the accumulation of turbidite lobes on the abyssal plain (Galloway et al., 2011; Sharman et al., 2017; Pecha et al., 2022). Early Eocene tectonic reorganisation shifted distributary systems southwest, with sediments entering the GoM mainly via the Colorado and Rio Grande, leaving the Mississippi axis in decline (Galloway et al., 2011; Sharman et al., 2017). The Upper Wilcox Group saw reduced sediment

supply due to Laramide basement unroofing and lacustrine basin development (Pecha et al., 2022). Notably, PETM climate shifts favoured floodplain clay transport (Foreman, 2014; Barefoot et al., 2022), bypassing the shelf by developing submarine canyons before being deposited in the GoM as the Yoakum Shale (Vimpere et al., 2023).

Despite these rearrangements, provenance studies show that the Wilcox Group was primarily sourced from the Western Cordillera and Laramide crystalline highlands in the central and southern Rockies (Sharman et al., 2017; Vimpere et al., 2023), and the ε_{Nd} record (Fig. 2f in main text) supports approximately constant provenance through time. A minor contribution of the Appalachian-Grenville provinces (Blum and Pecha, 2014) indicates reworking of older sediments in the eastern interiors (Sharman et al., 2017), potentially serving as CO_2 sources (Zondervan et al., 2023).

Paleogeographic reconstructions for the late Paleocene-early Eocene (Fig. 1 in main text) identify that three primary parent lithologies supplied sediments to the GoM during the PETM: (1) the Laramide and Appalachian basement (76% of eroded area); (2) Laramide sedimentary basins (23%); and (3) Paleogene volcanics (1%) (Fig. S2). At a global scale, shales are the primary sedimentary rock contributing to the Li budget (Dellinger et al., 2017). Given the distinctive high Li concentrations and low δ^7Li values in shales and granites compared to basalts, we applied a constant parent lithology correction that accounts for 77% igneous versus 23% shale source material. Using the lithological end-members from Ramos et al. (2022), with δ^7Li_{shale} = 0.3‰ and $\delta^7Li_{igneous}$ = 5.1‰, and assuming comparable Li concentrations in both end-members, we calculate the source composition (δ^7Li_{source}) to be 4.0‰. Hence, we obtain a pre-PETM $\Delta^7Li_{detrital\text{-}source}$ of -1.8±0.2‰, syn-PETM -2.2±0.3‰, recovery -3.3±0.2‰, and post-PETM -2.8±0.5‰. Given that the end members were measured within the catchment delivering sediments to the GoM, the area-weighted composition is expected to reflect the

average bedrock lithology well. We further assume a constant sediment provenance through time, and hence a constant δ^7Li_{source}, which is supported by the minimal variations in detrital Nd isotopes through the record (Fig. 2f and 3a in main text), and their lack of co-variation with the Li isotope changes (Fig. 3a in main text).

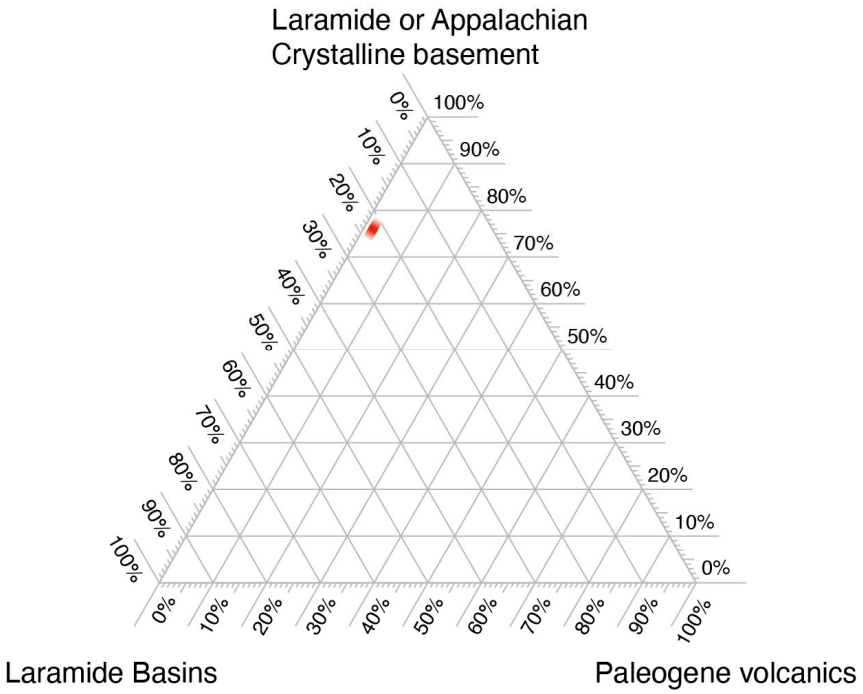

Figure S2. *Endmember bedrock lithology composition based on Figure 1 in the main text, modified after Sharman et al., (2017, 2023). We estimate the source lithology from the areas in the figure as (1) the Laramide and Appalachian basement, 76 %; (2) Laramide basins, 23 %; and (3) Paleogene volcanics, 1 % of the area.*

REFERENCES CITED

Barefoot, E.A., Nittrouer, J.A., Foreman, B.Z., Hajek, E.A., Dickens, G.R., Baisden, T., and Toms, L., 2022, Evidence for enhanced fluvial channel mobility and fine sediment export due to precipitation seasonality during the Paleocene-Eocene thermal maximum: v. 50, p. 116–120, doi:10.1130/G49149.1.

Blaser, P., Lippold, J., Gutjahr, M., Frank, N., Link, J.M., and Frank, M., 2016, Extracting foraminiferal seawater Nd isotope signatures from bulk deep sea sediment by chemical leaching: Chemical Geology, v. 439, p. 189–204, doi:10.1016/j.chemgeo.2016.06.024.

Blum, M., and Pecha, M., 2014, Mid-Cretaceous to Paleocene North American drainage reorganization from detrital zircons: Geology, v. 42, p. 607–610, doi:10.1130/G35513.1.

Bouchez, J., Von Blanckenburg, F., and Schuessler, J.A., 2013, Modeling novel stable isotope ratios in the weathering zone: American Journal of Science, v. 313, p. 267–308, doi:10.2475/04.2013.01.

Chen, Z., Ding, Z., Yang, S., Sun, J., Zhu, M., Xiao, Y., Tong, F., and Liang, Y., 2023, Strong Coupling Between Carbon Cycle, Climate, and Weathering During the Paleocene-Eocene Thermal Maximum: Geophysical Research Letters, v. 50, p. e2023GL102897, doi:10.1029/2023GL102897.

Dellinger, M., Bouchez, J., Gaillardet, J., Faure, L., and Moureau, J., 2017, Tracing weathering regimes using the lithium isotope composition of detrital sediments: Geology, v. 45, p. 411–414, doi:10.1130/G38671.1.

Dellinger, M., Gaillardet, J., Bouchez, J., Calmels, D., Louvat, P., Dosseto, A., Gorge, C., Alanoca, L., and Maurice, L., 2015, Riverine Li isotope fractionation in the Amazon River basin controlled by the weathering regimes: Geochimica et Cosmochimica Acta, v. 164, p. 71–93, doi:10.1016/j.gca.2015.04.042.

Foreman, B.Z., 2014, Climate-driven generation of a fluvial sheet sand body at the Paleocene-Eocene boundary in north-west Wyoming (USA): Basin Research, v. 26, p. 225–241, doi:10.1111/bre.12027.

Galloway, W.E., Whiteaker, T.L., and Ganey-Curry, P., 2011, History of Cenozoic North American drainage basin evolution, sediment yield, and accumulation in the Gulf of Mexico basin: Geosphere, v. 7, p. 938–973, doi:10.1130/GES00647.1.

Heller, P.L., and Liu, L., 2016, Dynamic topography and vertical motion of the U.S. Rocky Mountain region prior to and during the Laramide orogeny: Geological Society of America Bulletin, v. 128, p. 973–988, doi:10.1130/B31431.1.

Jones, M.T. et al., 2023, Tracing North Atlantic volcanism and seaway connectivity across the Paleocene–Eocene Thermal Maximum (PETM): Climate of the Past, v. 19, p. 1623–1652, doi:10.5194/cp-19-1623-2023.

Liu, C.-Y., Wilson, D.J., Hathorne, E.C., Xu, A., and Pogge Von Strandmann, P.A.E., 2023, The influence of river-derived particles on estuarine and marine elemental cycles: Evidence from lithium isotopes: Geochimica et Cosmochimica Acta, v. 361, p. 183–199, doi:10.1016/j.gca.2023.08.015.

Liu, Y., Yang, Y., Yan, Z., Jin, Z., Ye, C., Pogge Von Strandmann, P.A.E., Deng, L., Liu, X., and Fang, X., 2025, Lithium isotopes as a chemical weathering proxy in lacustrine sediments: Implications from multiphase leaching analyses: Global and Planetary Change, v. 253, p. 104986, doi:10.1016/j.gloplacha.2025.104986.

Pecha, M.E., Blum, M.D., Gehrels, G.E., Sundell, K.E., Karlstrom, K.E., Gonzales, D.A., Malone, D.H., and Mahoney, J.B., 2022, Linking the Gulf of Mexico and Coast Mountains batholith during late Paleocene time: Insights from Hf isotopes in detrital zircons, *in* Craddock, J.P., Malone, D.H., Foreman, B.Z., and Konstantinou, A. eds., Tectonic Evolution of the Sevier-Laramide Hinterland, Thrust Belt, and Foreland, and Postorogenic Slab Rollback (180–20 Ma), Geological Society of America, p. 265–292, doi:10.1130/2021.2555(10).

Pistiner, J.S., and Henderson, G.M., 2003, Lithium-isotope fractionation during continental weathering processes: Earth and Planetary Science Letters, v. 214, p. 327–339, doi:10.1016/S0012-821X(03)00348-0.

Pogge von Strandmann, P.A.E., Burton, K.W., Opfergelt, S., Genson, B., Guicharnaud, R.A., and Gislason, S.R., 2021a, The lithium isotope response to the variable weathering of soils in Iceland: Geochimica et Cosmochimica Acta, v. 313, p. 55–73, doi:10.1016/j.gca.2021.08.020.

Pogge von Strandmann, P.A.E., Cosford, L.R., Liu, C.-Y., Liu, X., Krause, A.J., Wilson, D.J., He, X., McCoy-West, A.J., Gislason, S.R., and Burton, K.W., 2023, Assessing hydrological controls on the lithium isotope weathering tracer: Chemical Geology, v. 642, p. 121801, doi:10.1016/j.chemgeo.2023.121801.

Pogge von Strandmann, P.A.E., Jenkyns, H.C., and Woodfine, R.G., 2013, Lithium isotope evidence for enhanced weathering during Oceanic Anoxic Event 2: Nature Geoscience, v. 6, p. 668–672, doi:10.1038/ngeo1875.

Pogge von Strandmann, P.A.E., Jones, M.T., West, A.J., Murphy, M.J., Stokke, E.W., Tarbuck, G., Wilson, D.J., Pearce, C.R., and Schmidt, D.N., 2021b, Lithium isotope evidence for enhanced weathering and erosion during the Paleocene-Eocene Thermal Maximum: Science Advances, v. 7, p. eabh4224, doi:10.1126/sciadv.abh4224.

Ramos, E.J. et al., 2024, Competition or collaboration: Clay formation sets the relationship between silicate weathering and organic carbon burial in soil: Earth and Planetary Science Letters, v. 628, p. 118584, doi:10.1016/j.epsl.2024.118584.

Ramos, E.J. et al., 2022, Swift Weathering Response on Floodplains During the Paleocene-Eocene Thermal Maximum: Geophysical Research Letters, v. 49, doi:10.1029/2021GL097436.

Rush, W., Zachos, J., Blackburn, T., and Pogge Von Strandmann, P.A.E., 2025, Continuous Sediment Sourcing and Changes in Weathering During the PETM in the Salisbury Embayment: Paleoceanography and Paleoclimatology, v. 40, p. e2025PA005116, doi:10.1029/2025PA005116.

Sharman, G.R., Covault, J.A., Stockli, D.F., Wroblewski, A.F.-J., and Bush, M.A., 2017, Early Cenozoic drainage reorganization of the United States Western Interior–Gulf of Mexico sediment routing system: Geology, v. 45, p. 187–190, doi:10.1130/g38765.1.

Sharman, G.R., Szymanski, E., Hackworth, R.A., Kahn, A.C.M., Febo, L.A., Oefinger, J., and Gregory, G.M., 2023, Carbon isotope chemostratigraphy, geochemistry, and biostratigraphy of the Paleocene–Eocene Thermal Maximum, deepwater Wilcox

Group, Gulf of Mexico (USA): Climate of the Past, v. 19, p. 1743–1775, doi:10.5194/cp-19-1743-2023.

Tanaka, T. et al., 2000, JNdi-1: a neodymium isotopic reference in consistency with LaJolla neodymium: Chemical Geology, v. 168, p. 279–281, doi:10.1016/S0009-2541(00)00198-4.

Vimpere, L. et al., 2023, Carbon isotope and biostratigraphic evidence for an expanded Paleocene–Eocene Thermal Maximum sedimentary record in the deep Gulf of Mexico: Geology, doi:10.1130/G50641.1.

Vimpere, L., et al., 2023, Supplementary Material for: Carbon isotope and biostratigraphic evidence for an expanded Paleocene–Eocene Thermal Maximum sedimentary record in the deep Gulf of Mexico: Geology, Supplementary Data File G50641_SuppMat.pdf.

Wei, G.-Y., Pohl, A., Jiang, S., Zhang, H., Wang, W., A. E. Pogge Von Strandmann, P., Maffre, P., Xiong, G., Shen, S., and Zhang, F., 2025, Changes in continental weathering regimes inhibited global marine deoxygenation during the Paleocene-Eocene thermal maximum: Nature Communications, v. 16, p. 9163, doi:10.1038/s41467-025-64217-0.

West, A., Galy, A., and Bickle, M., 2005, Tectonic and climatic controls on silicate weathering: Earth and Planetary Science Letters, v. 235, p. 211–228, doi:10.1016/j.epsl.2005.03.020.

Wilson, D.J., Pogge von Strandmann, P.A.E., White, J., Tarbuck, G., Marca, A.D., Atkinson, T.C., and Hopley, P.J., 2021, Seasonal variability in silicate weathering signatures recorded by Li isotopes in cave drip-waters: Geochimica et Cosmochimica Acta, v. 312, p. 194–216, doi:10.1016/j.gca.2021.07.006.

Winnick, M.J., Druhan, J.L., and Maher, K., 2022, Weathering intensity and lithium isotopes: A reactive transport perspective: American Journal of Science, v. 322, p. 647–682, doi:10.2475/05.2022.01.

Zarra, L., 2017, Chronostratigraphic framework for the Wilcox Formation (upper Paleocene–lower Eocene) in the deep-water Gulf of Mexico: Biostratigraphy, sequences, and depositional systems, in Kennan, L., et al., eds.,: The Paleogene of the Gulf of Mexico and Caribbean Basins: Processes, Events and Petroleum Systems: SEPM (Society for Sedimentary Geology) Gulf Coast Section SEPM Foundation 27, p. 81–145, doi:https:// doi.org/10.5724/gcs.07.27.0081.

Zondervan, J.R., Hilton, R.G., Dellinger, M., Clubb, F.J., Roylands, T., and Ogrič, M., 2023, Rock organic carbon oxidation CO2 release offsets silicate weathering sink: Nature, doi:10.1038/s41586-023-06581-9.

Table S1 *Geochemical records of C, Nd, and Li isotopes from Logan Walker Ridge WR 969#1 ST0. Depth in feet, depth in metres, $\delta^{13}C$ from Vimpere et al. (2023), ε_{Nd} values and two standard deviation (2sd) uncertainty, $\delta^{7}Li$ values and 2sd uncertainty.*

Depth (ft)	Depth (m)	$\delta^{13}C$	ε_{Nd}	2sd	$\delta^{7}Li$	2sd
27140	8272	-27.5	-12.7	0.1	1.4	0.4
27080	8254	-27.4	-13.6	0.1	2.3	0.5
27040	8242	-27.6	-13.1	0.1		
26930	8208	-27.6	-12.7	0.1		
26960	8217				2.4	0.0
26880	8193	-28.8	-12.2	0.1	2.0	0.1
26800	8169	-28.3	-11.6	0.1		
26770	8159	-29.1	-10.6	0.1	1.6	0.2
26740	8150	-29.2	-10.8	0.1	1.7	0.1
26720	8144	-29.2	-12.5	0.1		
26640	8120	-28.8	-13.4	0.1	1.9	0.4
26510	8080	-28.4	-13.0	0.1	1.6	0.4
26460	8065	-29.0	-16.0	0.1	2.3	0.3
26410	8050				0.6	0.5
26360	8035	-28.7	-14.3	0.1	0.9	0.4
26260	8004	-28.4	-13.9	0.1	1.0	0.1
26220	7992	-27.7	-14.6	0.1		
26190	7983	-27.7	-14.2	0.1	0.7	0.4
26100	7955	-27.9	-13.6	0.1	0.6	0.3
26070	7946	-27.8	-14.1	0.1		
26030	7934	-27.7	-14.3	0.1	0.5	0.1
25900	7894	-27.8	-14.1	0.1	1.9	0.5
25800	7864	-28.3	-12.1	0.1	1.0	0.1
25690	7830	-29.6	-11.7	0.2	0.9	0.2
26070	7946	-27.8	-14.3	0.1		